

Phase encoding in parametric nanomechanical resonator via annealing

Chen Yang(杨晨), Feng-Nan Chen(陈凤楠), Bo Wu(吴博), Ting-Ting Li(李婷婷), Zong-Yi Bao(鲍宗壹), Joel Moser, and Heng Lu(卢恒)

Citation: Chin. Phys. B, 2026, 35 (**7**): 074601. DOI: 10.1088/1674-1056/ae1def
http://cpb.iphy.ac.cn; http://iopscience.iop.org/cpb

What follows is a list of articles you may be interested in

Elastic-plastic behavior of nickel-based single crystal superalloys with *γ*-*γ′* phases based on molecular dynamics simulations

Jing-Zhao Cao(曹景昭), Yun-Guang Zhang(张云光), Zhong-Kui Zhang(张中奎), Jiang-Peng Fan(范江鹏), Qi Dong(董琪), and Ying-Ying Fang(方盈盈)

Chin. Phys. B, 2025, 34 (**4**): 046204. DOI: 10.1088/1674-1056/adb40f

Atomistic evaluation of tension—compression asymmetry in nanoscale body-centered-cubic AlCrFeCoNi high-entropy alloy

Runlong Xing(邢润龙) and Xuepeng Liu(刘雪鹏)

Chin. Phys. B, 2024, 33 (**1**): 016202. DOI: 10.1088/1674-1056/acfc37

Size effect on transverse free vibrations of ultrafine nanothreads

Zhuoqun Zheng(郑卓群), Han Li(李晗), Zhu Su(宿柱), Nan Ding(丁楠), Xu Xu(徐旭),Haifei Zhan(占海飞), and Lifeng Wang(王立峰)

Chin. Phys. B, 2023, 32 (**9**): 096202. DOI: 10.1088/1674-1056/ace037

Layer thickness dependent plastic deformation mechanism in Ti/TiCu dual-phase nano-laminates

Minrong An(安敏荣), Yuefeng Lei(雷岳峰), Mengjia Su(宿梦嘉), Lanting Liu(刘兰亭), Qiong Deng(邓琼), Haiyang Song(宋海洋), Yu Shang(尚玉), and Chen Wang(王晨)

Chin. Phys. B, 2023, 32 (**6**): 066201. DOI: 10.1088/1674-1056/acb48f

Numerical analysis of the resonance mechanism of the lumped parameter system model for acoustic mine detection

Wang Chi (王驰), Zhou Yu-Qiu (周瑜秋), Shen Gao-Wei (沈高炜), Wu Wen-Wen (吴文雯), Ding Wei (丁卫)

Chin. Phys. B, 2013, 22 (**12**): 124601. DOI: 10.1088/1674-1056/22/12/124601

Phase encoding in parametric nanomechanical resonator via annealing

Chen Yang(杨晨)[1,2,3,†], Feng-Nan Chen(陈凤楠)[1,2,3,†], Bo Wu(吴博)[1,2,3], Ting-Ting Li(李婷婷)[1,2,3], Zong-Yi Bao(鲍宗壹)[1,2,3], Joel Moser[1,2,3,‡], and Heng Lu(卢恒)[1,2,3,4,§]

[1] *School of Optoelectronic Science and Engineering and Collaborative Innovation Center of Suzhou Nano Science and Technology, Soochow University, Suzhou* 215006, *China*

[2] *Key Laboratory of Advanced Optical Manufacturing Technologies of Jiangsu Province and Key Laboratory of Modern Optical Technologies of Education Ministry of China, Soochow University, Suzhou* 215006, *China*

[3] *Jiangsu Key Laboratory of Flexible Optoelectronics and Micro-Nano Manufacturing, Suzhou* 215006, *China*

[4] *School of Optical and Electronic Information and Jiangsu Suzhou Key Laboratory of Biophotonics, Suzhou City University, Suzhou* 215006, *China*

(Received 30 September 2025; revised manuscript received 6 November 2025; accepted manuscript online 11 November 2025)

Nanomechanical resonators driven parametrically enable binary information encoding based on the control of their two possible vibrational phases. We present a protocol to flip the parametric phase in a graphene nanomechanical resonator via annealing, offering a novel approach to nanomechanical logic. The core of our methodology involves driving the resonator with a parametric excitation near twice its resonant frequency and applying an external drive to break the symmetry of the dynamical double-well potential of the bistable states. By introducing white force noise to anneal the resonator, its vibrational phase settles into the state with the lower potential. The phase can be deterministically prepared in one of two states, differing by approximately π radians, by controlling the phase of direct drive and annealing. The demonstrated protocol offers a promising approach for nanomechanical logic with potential advantages in efficiency, error resilience, and scalability.

Keywords: phase encoding, parametric amplification, mechanical resonator, graphene

PACS: 46.40.Ff, 62.25.–g, 62.40.+I, 05.45.–a

DOI: 10.1088/1674-1056/ae1def **CSTR:** 32038.14.CPB.ae1def

1. Introduction

Mechanical parametric resonance refers to the phenomenon in which a mechanical resonator exhibits large-amplitude oscillations induced by the periodic modulation of its spring constant, provided that the modulation strength exceeds a certain threshold.[1,2] This actuation mechanism has been employed for mechanical amplification[3–5] and is most effective when the modulation frequency is twice the resonant frequency of the fundamental vibrational mode f_0.[6–11] A canonical example is the pendulum with a periodically varying length.[12–14] Mechanical parametric resonance in resonators yields two accessible vibrational states characterized by degenerate amplitudes but phases differing by π.[15–18] In mechanical resonators, there exists a 50% probability that the system oscillates in either of the two parametric states.[17,19] To exert control over these phase states, an additional direct drive near the natural resonance frequency is applied, serving as a symmetry-breaking force.[17,20,21] The parametric phase-encoded logic is protected by a phase gap of π, which is attractive for advanced and reliable computation. Various phase control techniques and phase encoding schemes have been developed. In micrometer-scale beams incorporating quantum wells actuated via the piezoelectric effect,[19] bit storage and bit flip operations are realized by manipulating the phase of mechanical oscillations through the application of pulse sequences and trigger switches. Prior to writing any bit, both the parametric and direct drives are turned off to initialize the oscillator at zero amplitude. Subsequently, a small driving force functions as a switch to control the state. Other researchers have introduced novel phase encoding schemes combining hardware carriers of levitated nanoparticles and electrical LC resonator circuits with the approach of controlling the underlying potential rapidly.[22] This approach enables rapid modulation of the underlying potential, representing a paradigm shift in phase-encoded logic operations by substantially enhancing the speed of parametron bit-flip processes. In graphene nanomechanical resonators, phase states can be manipulated by adjusting a DC gate voltage in the presence of the parametric excitation and the drive.[23] Instead of sweeping the frequency of the direct drive f_d and the parametric pump f_p, applying a DC bias V_g^dc between the graphene membrane and an underlying gate electrode tunes tensile strain within the membrane, thereby tuning ω_0, and transitioning the resonator

†These authors contributed equally to this work.

‡Corresponding author. E-mail: j.moser@suda.edu.cn

§Corresponding author. E-mail: luheng@szcu.edu.cn

© 2026 Chinese Physical Society and IOP Publishing Ltd. All rights, including for text and data mining, AI training, and similar technologies, are reserved.

into and out of parametric resonance. Whether the pump frequency is swept from below or from above parametric resonance determines the subsequent parametric phase state. This technique allows phase state flipping through simple adjustments of the DC voltage; however, it necessitates adiabatic transitions into and out of parametric resonance.

In this paper, we explore a method to manipulate the vibrational phase in a parametric graphene resonator. Our method is based on the annealing of the phase states in a double-well pseudo-potential with broken symmetry. By applying an external drive frequency near the natural resonance frequency f_0, we induce symmetry breaking in the dynamical double-well potential associated with the Hamiltonian governing the bistable states arising from parametric excitation at $2f_0$.[24–27] The energy barrier separating these bistable states is modulated through adjustments in either the amplitude or the phase θ (with respect to the pump) of the driving force.[17] In a scenario where the double-well potential exhibits asymmetry, we introduce white force noise to anneal the oscillator, thereby stabilizing it into the lowest energy phase state. Notably, this phase transition is reversible only by inverting the potential landscape and repeating the annealing process. Compared to previously reported techniques, our protocol offers the advantage of flipping binary phase bits without necessitating intermediate transition states for resetting, nor requiring frequency sweeps of the drive or gate voltage modulation, thereby enhancing operational efficiency. Furthermore, the phase bit in our approach is strongly dependent on θ, obviating the need for additional decision-making regarding phase retention or inversion for subsequent phase bits based on the initial phase. This characteristic also mitigates the propagation of errors, as a single error does not induce cascading failures. Additionally, the feasibility of fabricating large-scale arrays of graphene devices on compact chips has been demonstrated,[28] underscoring the scalability of our approach. Overall, our findings present an alternative strategy for the manipulation of nanomechanical phase bits.

2. Theoretical model

The fundamental concept underlying phase encoding is exemplified by the parametron.[29,30] A first-order parametric resonance can be excited by modulating the spring constant of a harmonic oscillator at twice its natural angular frequency $\omega_p = 2\omega_0$. In contrast, a conventional harmonic resonance occurs when the oscillator is driven at its natural angular frequency $\omega_d = \omega_0$.[31] Near the natural frequency, the parametric resonance exhibits bistability (green region in Fig. 1(a)). The two resultant states possess identical amplitude and period, but their phases differ by π radians.[32] Consequently, the oscillator can stably occupy one of two phase states, designated as 0 and 1, thereby facilitating the implementation of bit storage and bit-flip operations.

Our methodology begins by incorporating a force noise term into the equation of motion governing a nonlinear, parametrically excited resonator:[18,20,33]

$$\ddot{z}+\Gamma\dot{z}+\frac{\alpha}{m_{\rm eff}}z^3+\frac{\eta}{m_{\rm eff}}z^2\dot{z}+\omega_0^2[1-\lambda\cos(\omega_{\rm p}t)]z=\frac{F_{\rm d}}{m_{\rm eff}}\cos(\omega_{\rm d}t+\theta)+\frac{\xi(t)}{m_{\rm eff}}, \tag{1}$$

where z is the amplitude of displacement in the flexural direction, dots on z represent derivatives with respect to time t, $\Gamma=\omega_0/Q$ with quality factor Q and resonant angular frequency $\omega_0=2\pi f_0$, α and η are the nonlinear conservative restoring force coefficient and the nonlinear dissipative force coefficient, respectively, $F_{\rm d}$ is the peak amplitude of the external direct driving force, $m_{\rm eff}$ is the effective mass of the fundamental vibration mode, $\omega_{\rm d}=2\pi f_{\rm d}$ is the angular frequency of drive force, $\omega_{\rm p}=2\pi f_{\rm p}$ is the angular frequency of parametric excitation, θ is the phase difference between the driving force and the parametric excitation, λ is the modulation strength of parametric pumping, and $\xi(t)$ is the fluctuating force noise.[34] In the simulations presented in Fig. 1, we employ parameters characteristic of graphene resonators operating at room temperature, specifically: $m_{\rm eff}=1.2\times10^{-16}$ kg, $\omega_0=2\pi\times 50.2\times10^6$ rad/s, $Q=81$, $\alpha=-4\times10^{16}$ kg/(m^2·s^2), $\eta=3.4\times10^7$ kg/(m^2·s) (see Appendix A). Figure 1(a) illustrates the amplitude of the two stable phase states, depicted in blue, which exhibit degeneracy in amplitude. Information encoding via these phase states is feasible within the green-shaded regions near the parametric drive frequency $f_{\rm p}=2f_0$. The parametric modulation strength is fixed at $\lambda=0.03$, while both the external driving force $F_{\rm d}$ and noise term $\xi(t)$ are set to zero. Figure 1(b) presents the stability diagram in the uv-plane, where u and v represent the in-phase and quadrature components of the resonator's displacement over the simulation period. The parametric drive frequency $f_{\rm p}$ is set to 100.4 MHz and the force noise variance $\langle\xi^2\rangle\simeq4.5\times10^{-20}$ N^2. This diagram indicates the most probable phase state of the resonator and corresponds to the stationary occupation probabilities $p_\uparrow$ and $p_\downarrow$. Under these conditions, the phase stochastically switches between the two states, yielding nearly equal occupation probabilities $p_\uparrow\simeq p_\downarrow\simeq0.5$, where the $\uparrow$ and $\downarrow$ phase states are designated as logical bits 1 and 0, respectively. The locations of the two phase states in the uv space can be rotated arbitrarily by changing the phase of the reference signal, but these states will retain a phase difference of π radians and will remain degenerate in amplitude, so their amplitude sym-

metry is unbroken. The amplitude symmetry of these states is broken by the application of an external force with magnitude $F_d = 2 \times 10^{-11}$ N and phase angle $\theta = -45°$, as depicted in Fig. 1(c). Here, the oscillator exhibits a preference for the ↑ phase state, with a stationary occupation probability $p_\uparrow \simeq 0.8$. Figure 1(d) presents the stationary occupation probability $p_\downarrow$ as a function of θ for various values of F_d ranging from 10^{-11} N to 6×10^{-11} N. An increase in F_d results in a sharper transition in $p_\downarrow(\theta)$ and enhances the stability of the phase within a specific state. We thus choose the parameters $F_d = 6 \times 10^{-11}$ N, $\theta_1 = -50°$, and $\theta_2 = -20°$ for simulations of phase state switching. If θ varies over a range of 0 $-360°$, two transitions are expected (see Appendix B). As depicted in Fig. 1(e), the parameter θ is initially set to $\theta_1 = -50°$ to configure the double-well potential under the combined effects of parametric modulation and an external force. Subsequently, noise is introduced for a short interval of 160 ms to heat up the resonator, thereby facilitating its transition toward the lower potential well phase state. After turning the noise off, the oscillator undergoes cooling and stabilizes in the ↑ state, maintaining phase stability thereafter. In the subsequent stage, θ is set to $\theta_2 = -20°$, effectively inverting the double-well potential such that the lower potential well corresponds to the ↓ state. Noise is again briefly applied and then switched off, enabling the oscillator to settle into the ↓ state. This procedure results in a reversed phase state, as demonstrated by the stability of the phase trajectory following the switching event. The schematic of the modifications in the double-well potential throughout this process is provided in Appendix C.

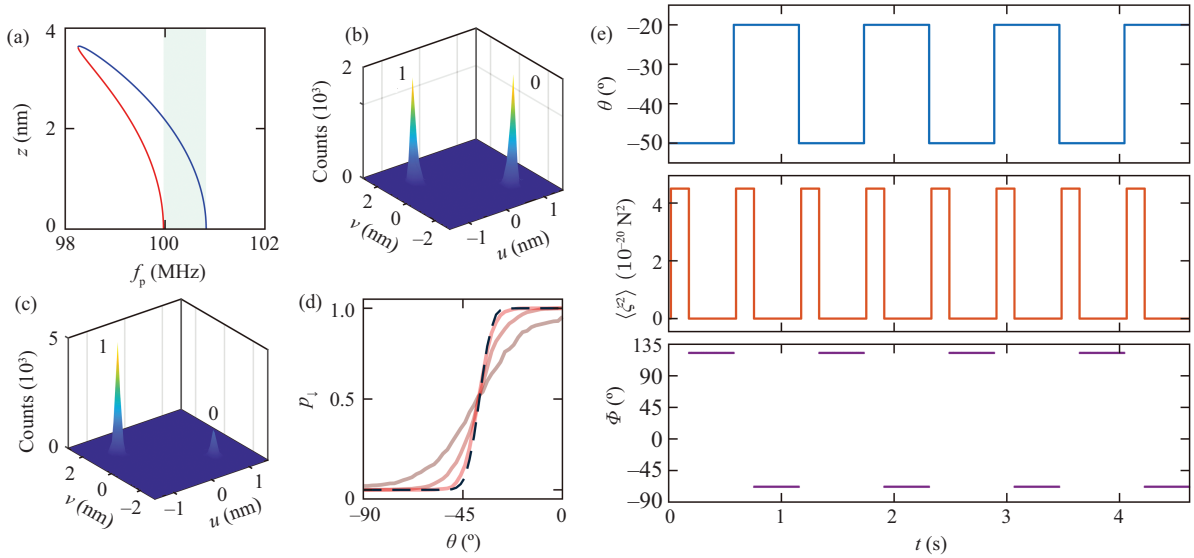


Fig. 1. Simulation of the phase encoding in a parametrically excited nanomechanical resonator. (a) Amplitude response z of the resonator calculated as a function of parametric pump frequency f_p by solving Eq. (1). $m_{eff} = 1.2 \times 10^{-16}$ kg, $\omega_0 = 2\pi \times 50.2 \times 10^6$ rad/s, $\Gamma = 3.9 \times 10^6$ rad/s, $\alpha = -4 \times 10^{16}$ kg/(m^2·s^2), $\eta = 3.4 \times 10^7$ kg/(m^2·s), $\lambda = 0.03$, $F_d = 0$, $\xi(t) = 0$. The red trace represents the unstable state. The shaded region highlights the range of f_p where there are only two stable phase states (blue branch representing the two amplitude-degenerate phase states). (b) Distribution of the in-phase and quadrature components of the displacement uv. $\langle\xi^2\rangle \simeq 4.5 \times 10^{-20}$ N^2, $\omega_d = 2\pi \times 50.2 \times 10^6$ rad/s, and $F_d = 0$ N. (c) uv distribution with same $\langle\xi^2\rangle$ and ω_d as in panel (b), $F_d = 2 \times 10^{-11}$ N, $\theta = -45°$. (d) Stationary occupation probabilities $p_\downarrow$ of the state ↓ as a function of θ with different values of F_d. From dark to light: $F_d = 10^{-11}$ N, 2×10^{-11} N, and 4×10^{-11} N, respectively. Black dashed line: $F_d = 6 \times 10^{-11}$ N. $\langle\xi^2\rangle$ and ω_d are same as panels (b) and (c). (e) Phase of the direct drive θ ($\theta_1 = -50°$, $\theta_2 = -20°$), noise variance $\langle\xi^2\rangle$, and vibrational phase Φ of the resonator as a function of time. The phase state is periodically flipped by tuning θ and $\langle\xi^2\rangle$.

3. Results and discussion

We proceed to experimentally validate our phase flip protocol. The device is a few-layer graphene nanomechanical resonator shaped as a $\sim 3-\mu$m diameter drum (this device has been previously utilized in Ref. [35]; however, all measurements reported herein are original). The membrane is suspended over a local gate electrode, which is patterned at the bottom of a cavity etched in SiO_2. The device is held in a vacuum of $\sim 10^{-5}$ mbar (1 bar $= 10^5$ Pa) at room temperature. The device is positioned within an optical standing wave formed between a wave plate and the gate electrode, which functions as a mirror.[36–40] An arbitrary waveform generator (AWG) outputs a composite voltage signal applied to the gate electrode ($\delta V_g = A_1 \cos(\omega_d t + \theta) + A_2 \cos(\omega_p t)$, where A_1 is the amplitude of the direct drive. A_2 and $\omega_p = 2\omega_d$ correspond to the amplitude and angular frequency of a secondary drive at twice the fundamental frequency, serving as an effective parametric pump.[10,25] Here, $A_{1,2}$ represent the peak amplitudes of the voltage waves at the gate. This composite waveform is applied together with a bias voltage V_g^{dc} to actuate the graphene membrane vibrations at frequency ω_d. The output voltage of the photodetector, measured in the reflected light path, oscillates at frequency ω_d, with its amplitude proportional to the vibrational amplitude of the membrane.[41–46] This signal is recorded using a high-frequency lock-in amplifier. As a refer-

ence, a sinusoidal voltage waveform with peak amplitude A_3 at frequency ω_d, generated by the same oscillator within the AWG, is utilized. Noise is introduced to the device source via an additional bias tee, whose DC port is terminated with a 50-Ω resistor to ground.

Figure 2(b) presents the amplitude of the resonator's linear response, quantified as the electrical power $R = 10 \times \log_{10}(V_{PD}^2/0.4)$ measured at the output of the photodetector as a function of drive frequency f_d and the gate voltage V_g^{dc}, with a drive power $P_d = -37$ dBm at the gate, and with $A_2 = 0$. R is in units of dBm and takes into account the output and input impedances in the setup. Figure 2(b) shows that the resonant frequency of the response is tunable with the gate voltage, and the fundamental vibrational mode is unambiguously defined in the spectrum.

The experimental validation of our protocol is presented in Figs. 2(c)–2(e). We quantify the stationary occupation probability of the ↓ phase state $p_\downarrow$ as a function of θ. Here, the noise variance $\langle \xi^2 \rangle$ is determined by integrating the power spectral density $S_{uu}(\omega)$ of the white voltage noise applied between the resonator and the gate over the noise bandwidth. Compared to the ideal simulation depicted in Fig. 1(d), the experimentally measured phases exhibit an additional offset attributable to wave propagation delays within the experimental setup. Given that the phase range of the lock-in amplifier is confined between $-\pi$ and π, a substantial offset may cause the $p_\downarrow(\theta)$ to invert vertically. However, this inversion does not invalidate the fundamental concept of employing bistable parametric states for encoding purposes. The resonator preferentially occupies the ↓ state for $\theta < -65°$, whereas it occupies the ↑ state for $\theta > -35°$. Accordingly, we select $\theta_1 = -75°$ and $\theta_2 = -25°$ to induce phase flipping, as illustrated in Fig. 2(d), where we plot θ, $\langle \xi^2 \rangle$, and the measured phase Φ as a function of time. The resulting phase has an expected phase difference of nearly π radians and is stable in time. Namely, we extract a flipping probability $P_{flip} = 1$, which is defined as the ratio of successful phase flips to the total flipping attempts[23] after two hundred flips with a noise trigger duration $\tau \simeq 100$ ms (the inset in Fig. 2(d)). For comparison, phase measurements conducted in the absence of added noise are shown in Fig.2(e). The noise level is set to the minimum value $\langle \xi^2 \rangle \simeq 8.6 \times 10^{-8}\ V_{rms}^2$ instead of switching the noise off entirely to mitigate the equipment communication delays. The resonator remains in its initial phase state throughout the modulation of θ, demonstrating that noise-induced annealing is a critical component of the protocol.

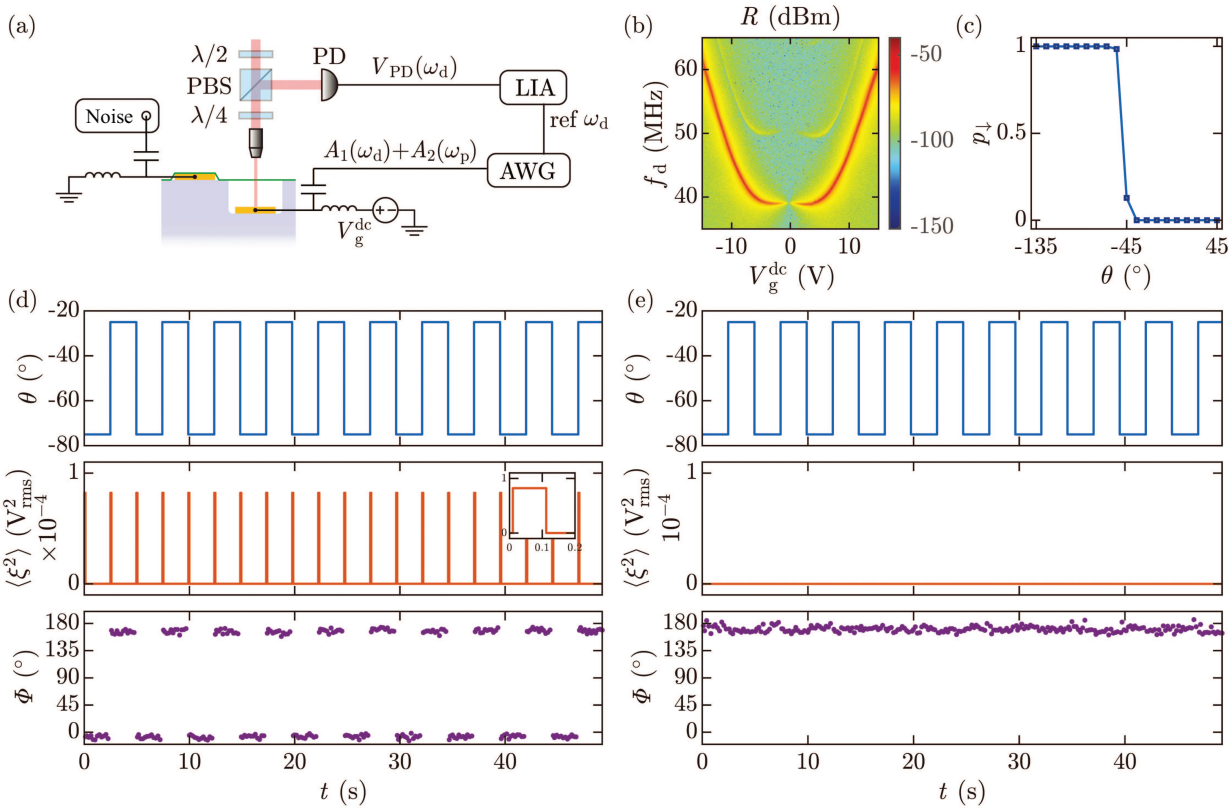


Fig. 2. Experimental demonstration of our phase encoding scheme. (a) Measurement setup. PD: photodetector; PBS: polarizing beam splitter; λ/2 and λ/4: half-wave and quarter-wave plate; FLG: few-layer graphene; LIA: lock-in amplifier; AWG: arbitrary waveform generator; A laser beam with wavelength of 633 nm is used. (b) Linear amplitude response of the resonator to a small direct drive measured as the electrical power $R = 10 \times \log_{10}(V_{PD}^2/0.4)$ at the output of the photodetector as a function of the drive frequency f_d and gate voltage V_g^{dc}. The power of the direct drive is $P_d = -37$ dBm. (c) Stationary occupation probabilities $p_\downarrow$ of the state ↓ as a function of θ. The noise variance $\langle \xi^2 \rangle \simeq 8.22 \times 10^{-5}\ V_{rms}^2$. (d)–(e) Phase of the direct drive θ ($\theta_1 = -75°$, $\theta_2 = -25°$), noise variance $\langle \xi^2 \rangle$ and vibrational phase Φ of the resonator as a function of the time. In panel (d), $\langle \xi^2 \rangle \simeq 8.22 \times 10^{-5}\ V_{rms}^2$, the trigger time $\tau = 100$ ms, as shown in the inset. In panel (e), $\langle \xi^2 \rangle \simeq 8.6 \times 10^{-8}\ V_{rms}^2$. $V_g^{dc} = 11$ V, $f_d \simeq 50.2$ MHz, $A_1 \simeq 7.1$ mV, $A_2 \simeq 0.71$ V in panels (c)–(e).

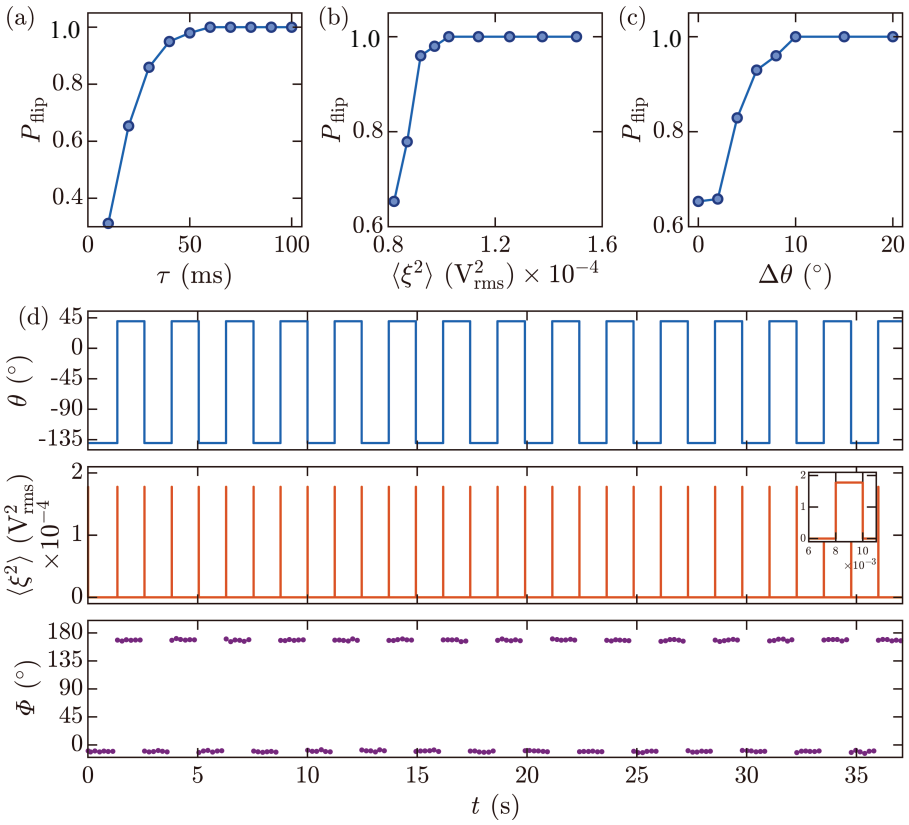


Fig. 3. Optimization of the flipping probability $P_{\rm flip}$. $P_{\rm flip}$ as a function of (a) the trigger time τ, (b) the noise intensity $\langle\xi^2\rangle$, and (c) the phase difference $\Delta\theta$. In panel (a), $\langle\xi^2\rangle \simeq 8.22\times10^{-5}\ V^2_{\rm rms}$, $\theta_1 = -75°$, $\theta_2 = -25°$. In panel (b), $\tau = 20$ ms, $\theta_1 = -75°$, $\theta_2 = -25°$. In panel (c), $\tau = 20$ ms, $\langle\xi^2\rangle \simeq 8.22\times10^{-5}\ V^2_{\rm rms}$. (d) Phase Φ of the resonator as a function of the time. $\theta_1 = -140°$, $\theta_2 = 40°$, $\langle\xi^2\rangle = 1.78\times10^{-4}\ V^2_{\rm rms}$, noise trigger time $\tau = 2$ ms shown in the inset. In all panels: $V_{\rm g}^{\rm dc} = 11$ V, $f_{\rm d} \simeq 50.2$ MHz, $A_1 \simeq 7.1$ mV, and $A_2 \simeq 0.71$ V.

Finally, we optimize the flipping probability $P_{\rm flip}$ of the phase flipping protocol by changing the trigger time τ, phase difference θ, and the noise intensity $\langle\xi^2\rangle$. Figure 3(a) presents the flipping probabilities of Φ for various trigger times τ. $P_{\rm flip}$ is calculated based on 200 flips and reaches ~ 1 when $\tau \geq 60$ ms. Given that $\tau \simeq 20$ ms in Fig. 3(a), $P_{\rm flip} \simeq 0.65$ is achieved after two hundred flip attempts. The first 30 seconds of the measurement data are shown in Appendix D. Figure 3(b) displays the dependence of $P_{\rm flip}$ on the noise intensity $\langle\xi^2\rangle$. An increase in noise intensity leads to an enhancement of $P_{\rm flip}$. This indicates that stronger noise levels enable the use of shorter τ. Nevertheless, care has to be taken upon increasing the noise because excessive noise induces stochastic transitions between the two states.[24,47] In Fig. 3(c), the flipping probability $P_{\rm flip}$ is calculated from the measured time evolution of Φ (200 periods) with $\theta_1 = -75° - \Delta\theta$ and $\theta_2 = -25° + \Delta\theta$. The larger $\Delta\theta$ means stronger symmetry breaking of the double-well potential.[19] Notably, the enlargement of phase difference between θ_1 and θ_2 also enhances $P_{\rm flip}$. This indicates that the trigger time could be shortened by tuning the energy barrier between two phase states. Figure 3(d) depicts the flipping of phase Φ as a function of time with a larger $\Delta\theta$ ($\theta_1 = -140°$, $\theta_2 = 40°$) but smaller noise trigger intensity ($\langle\xi^2\rangle \times \tau = 3.56\times10^{-4}\ V^2_{\rm rms}\cdot$ms) compared to Fig. 2(d). The flipping probability $P_{\rm flip} = 1$ is measured within continuous 500 flips. In contrast to the approach in which the gate voltage is varied sufficiently slowly to ensure an adiabatic state transition,[23] flipping the phase states using an uncorrelated force noise is a nonadiabatic, out-of-equilibrium process. Indeed, the occupation probability of a given state depends on the transition rates out of both states, which are thermally activated.[48–51] The stochastic nature of the interstate transitions also implies that the burst of force noise should be long enough to guarantee that the state is flipped. We have found that the minimum duration $\tau \simeq 2$ ms of the burst yielding $P_{\rm flip} \simeq 1$ is still significantly larger than both the period of vibrations $1/f_0 \simeq 2\times10^{-8}$ s and the ringdown time $Q/f_0 \simeq 1.6\times10^{-6}$ s, two fundamental time limits in rapid phase flip protocols.[19,22] Therefore, while our process operates more rapidly than an adiabatic gate voltage sweep, it remains considerably slower than the most rapid phase flip protocols.

4. Conclusion

In summary, we have developed and experimentally demonstrated a phase encoding protocol for graphene nanomechanical resonators. While earlier works have focused on manipulating the phonon populations of strongly coupled nanomechanical modes with microwave pulses at cryogenic temperatures,[52–54] we focus on manipulating parametric phase states with noise bursts at room temperature. Our encoding is classical. Namely, we cannot create a state based

on the superposition of the two phase states; it is either one or the other. In this sense, our method is less versatile and is more the mechanical equivalent of classical bit encoding. The resonator is parametrically excited, resulting in a symmetric bistable system which is subsequently perturbed by the application of an external direct driving force. Building upon this framework, we integrate annealing with white force noise and implement phase control between the direct drive and parametric excitation to select the phase state. The compact dimensions of the device facilitate high-density integration on a single chip, while the low mass of graphene enables operation with minimal power consumption. Additionally, the extensive frequency tunability of the graphene resonator supports both coupling between adjacent devices and effective isolation.[55] Moreover, the dynamical double-well potential enhances phase stability by mitigating the effects of phase noise.[56] The pronounced sensitivity of the energy landscape and phase bits to the phase difference between the driving force and parametric excitation effectively prevents the propagation of chain errors. The methodology presented here could be extended to other two-dimensional materials, including MoS_2, which exhibits higher quality factors at low temperature due to the large energy gap in the phonon dispersion that reduces energy dissipation.[57,58] In addition, our work holds promise for future applications, including nanoelectromechanical logic circuits and network systems.

Appendix A: Response of resonator with the direct drive and with the parametric pump

The linear response of the resonator without the parametric pump, measured as the electrical power R at the output of the photodetector as a function of drive frequency f_d, is illustrated in Fig. A1(a). The response $V_{PD}(\omega_d) = \kappa z(\omega_d)$ (blue curve), fitted with a linear transduction factor κ, yields key mechanical parameters: quality factor $Q \simeq 81$, effective mass of resonator $m_{eff} \simeq 3.4 \times 10^{-16}$ kg, and resonant frequency $f_0 \simeq 50.2$ MHz. The quality factor of the resonator can be improved by cooling the device to low temperatures[28,59] or by using twisted bilayer graphene membranes.[60] Figure A1(b) illustrates the nonlinear response of the resonator under parametric pumping. The blue and red curves correspond to measurements taken during increasing and decreasing drive frequency sweeps, respectively. Fitting the data (orange curve) allows estimation of the nonlinear coefficients: nonlinearities $\alpha \simeq -4 \times 10^{16}$ kg/(m^2·s^2), $\eta \simeq 3.4 \times 10^7$ kg/(m^2·s). Figures A1(c) and A1(d) show the measured power R as a function of driving frequency ($f_d = f_p/2$) and the parametric excitation voltage (A_2), in the absence of an external drive. The drive frequency is swept upward in Fig. A1(c) and downward in Fig. A1(d). A threshold parametric excitation amplitude $A_{2,th} \simeq 0.57$ V is identified, above which parametric resonance emerges.

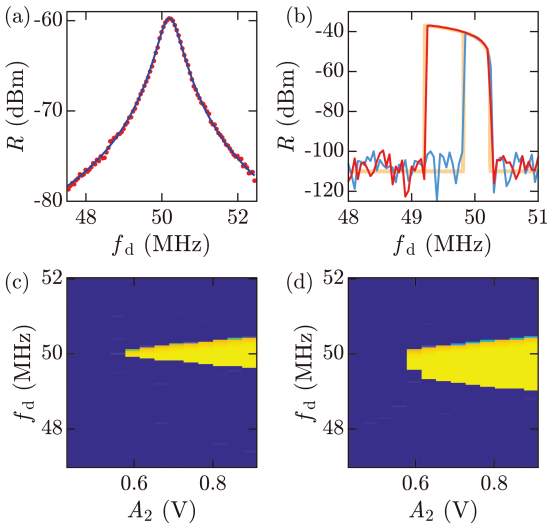


Fig. A1. Response of the resonator: (a) Linear amplitude response of the resonator to a small direct drive measured as the electrical power $R = 10 \times \log_{10}(V_{PD}^2/0.4)$ at the output of the photodetector as a function of f_d (red dotted line). $V_g^{dc} = 11$ V, $P_d = -37$ dBm. Blue curve: fitted by the linear motion equation of resonator, where $m_{eff} \simeq 3.4 \times 10^{-16}$ kg, $f_0 \simeq 50.2$ MHz, $\Gamma \simeq 3.9 \times 10^6$ rad/s. (b) Parametric response measured as the power R as a function of f_d swept increased (blue curve) and decreased (red curve). $V_g^{dc} = 11$ V, $A_1 \simeq 0$ V, $A_2 \simeq 0.7$ V. Orange curve: fitted by Eq. (1), where $\alpha \simeq -4 \times 10^{16}$ kg/(m^2·s^2), $\eta \simeq 3.4 \times 10^7$ kg/(m^2·s). Parametric vibrational amplitude measured as the power R as a function of A_2 when f_d (c) increases and (d) decreases respectively. $V_g^{dc} = 11$ V, power scale: -100 dBm (blue) to -40 dBm (yellow).

Appendix B: Calculated $p_\downarrow(\theta)$ as a function of θ over the interval of 0°–360°

With $F_d = 6 \times 10^{-11}$ N in Fig. 1(d), $p_\downarrow$ as a function of θ over the interval of 0°–360° is shown in Fig. B1. This function exhibits a periodicity of 360°. θ_1 and θ_2 can be selected to result in $p_\downarrow(\theta) \simeq 0$ and $p_\downarrow(\theta) \simeq 1$, respectively.

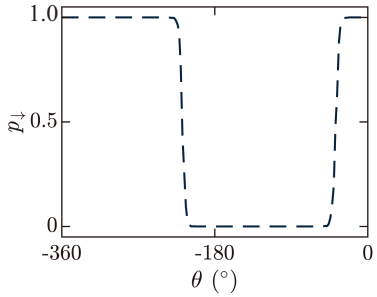


Fig. B1. Calculated stationary occupation probabilities $p_\downarrow$ of the state $\downarrow$ as a function of θ with $F_d = 6 \times 10^{-11}$ N, $\langle \xi^2 \rangle \simeq 4.5 \times 10^{-20}$ N^2 and $\omega_d/2\pi = 50.2$ MHz. Other parameters are the same as in Fig. 1(d), $m_{eff} = 1.2 \times 10^{-16}$ kg, $\omega_0/2\pi = 50.2$ MHz, $\Gamma = 3.9 \times 10^6$ rad/s, $\alpha = -4 \times 10^{16}$ kg/(m^2·s^2), $\eta = 3.4 \times 10^7$ kg/(m^2·s), $\lambda = 0.03$.

Appendix C: Schematic depicting the tuning the double well potential of the system in our phase encoding protocol

Figure C1 illustrates the evolution of the resonator, including its initial condition prior to phase encoding. Initially, when only parametric excitation is applied, the double-well potential is symmetric, and the resonator resides in one of the

two phase states separated by a saddle point. Each state has an equal probability of 50% (stage I). The introduction of an external driving force with a the phase θ_1 breaks the symmetry in the dynamic double-well potential, resulting in a phase state settling at a lower potential and thus becoming energetically favored. Following annealing through the application of noise, the resonator transitions into the lower potential state and remains there after the noise is turned off (stage II). This behavior can be reversed by adjusting the phase from θ_1 to θ_2, which lowers the potential of the opposite phase state. After subsequent annealing, the resonator again transitions to the lower potential state, but with its phase inverted (stage III). Successive phase encoding processes correspond to iterative transitions between stages II and III.

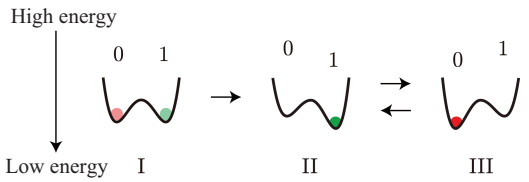


Fig. C1. Schematic diagram of tuning the double well potential of the system in our phase encoding protocol. Stage I: external direct drive is off. Stage II: external direct drive is on with a phase of θ_1. Stage III: external direct drive is on with a phase of θ_2.

Appendix D: Flipping phase states with $P_{\text{flip}} < 1$

In the case of $\tau \simeq 20$ ms in Fig. 3(a), $P_{\text{flip}} \simeq 0.65$ after two hundred flip attempts. The measured Φ within the first 30 seconds is shown in Fig. D1.

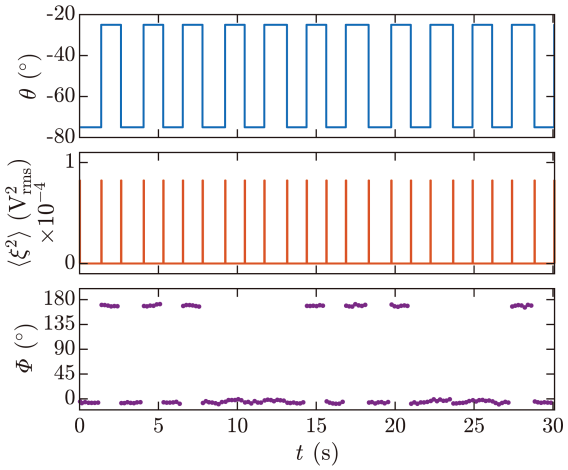


Fig. D1. Phase of the direct drive θ ($\theta_1 = -75°$, $\theta_2 = -25°$), force noise variance $\langle \xi^2 \rangle$, and measured phase Φ of the resonator as a function of time. The trigger time τ is set to 20 ms. $V_{\text{g}}^{\text{dc}} = 11$ V, $f_{\text{d}} \simeq 50.2$ MHz, $A_1 \simeq 7.1$ mV, $A_2 \simeq 0.71$ V.

Acknowledgments

Project supported by the National Natural Science Foundation of China (Grant Nos. 62150710547 and 62074107) and the Project of the Priority Academic Program Development (PAPD) of Jiangsu Higher Education Institutions. We thank Prof. Wang Chinhua for the strong support. The authors are grateful to Alexander Eichler from the ETH Zurich for inspiring discussion.

References

[1] Thurnher T, Haller G and Jain S 2024 *Chaos* **34** 073127
[2] Frangi A, Guerrieri A, Carminati R and Mendicino G 2017 *IEEE Transactions on Industrial Electronics* **64** 1544
[3] Mathew J P, Patel R N, Borah A, Vijay R and Deshmukh M M 2016 *Nature Nanotech.* **11** 747
[4] Singh R, Nicholl R J, Bolotin K I and Ghosh S 2018 *Nano Lett.* **11** 6719
[5] Su Z J, Ying Y, Song X X, Zhang Z Z, Zhang Q H, Cao G, Li H O, Guo G C and Guo G P 2021 *Nanotechnology* **32** 155203
[6] Turner K L, Miller S A, Hartwell P G, MacDonald N C, Strogatz S H and Adams S G 1998 *Nature* **396** 149
[7] Carr D W, Evoy S, Sekaric L, Craighead H G and Parpia J M 2000 *Appl. Phys. Lett.* **77** 1545
[8] Butikov E I 2004 *Eur. J. Phys.* **25** 535
[9] Karabalin R B, Masmanidis S C and Roukes M L 2010 *Appl. Phys. Lett.* **97** 183101
[10] Eichler A, Chaste J, Moser J and Bachtold A 2011 *Nano Lett.* **11** 2699
[11] Melkani A and Paulose J 2024 *Phys. Rev. E* **110** 015003
[12] Magazu S and Caccamo M T 2024 *Sci. Rep.* **14** 24657
[13] Chikmagalur K and Bamieh B 2025 *IEEE Transactions on Control of Network Systems* **12** 2254
[14] Jia Y, Du S and Seshia A A 2016 *Sci. Rep.* **6** 30167
[15] Lifshitz R and Cross M C 2008 *Nonlinear dynamics of nanomechanical and micromechanical resonators* (Weinheim: Wiley-VCH) pp. 1–52
[16] Dykman M I 2012 *Fluctuating Nonlinear Oscillators: From Nanomechanics to Quantum Superconducting Circuits* (Oxford: Oxford Academic)
[17] Mahboob I, Froitier C and Yamaguchi H 2010 *Appl. Phys. Lett.* **96** 213103
[18] Papariello L, Zilberberg O, Eichler A and Chitra R 2016 *Phys. Rev. E* **94** 022201
[19] Mahboob I and Yamaguchi H 2008 *Nat. Nanotech.* **3** 275
[20] Leuch A, Papariello L, Zilberberg O, Degen C L, Chitra R and Eichler A 2016 *Phys. Rev. Lett.* **117** 214101
[21] Nosan Z, Marki P, Hauff N, Knaut C and Eichler A 2019 *Phys. Rev. E* **99** 062205
[22] Frimmer M, Heugel T L, Nosan Z, Tebbenjohanns F, Halg D, Akin A, Degen C L, Novotny L, Chitra R, Zilberberg O and Eichler A 2019 *Phys. Rev. Lett.* **123** 254102
[23] Yang C, Zhang Y B, Lu H, Zhang C, Chen F N, Yan Y, Xue F, Eichler A and Moser J 2025 *Phys. Rev. Appl.* **23** 054036
[24] Ryvkine D, Dykman M I 2006 *Phys. Rev. E* **74** 061118
[25] Eichler A and Zilberberg O 2023 *Classical and Quantum Parametric Phenomena* (Oxford: Oxford Academic)
[26] Dumont V, Bestler M, Catalini L, Margiani G, Zilberberg O and Eichler A 2024 *Phys. Rev. Research* **6** 043012
[27] Woo J and Landauer R 1971 *IEEE Journal of Quantum Electronics* **7** 435
[28] Zande A M, Barton R A, Alden J S, Ruiz-Vargas C S, Whitney W S, Pham P H, Park J, Parpia J M, Craighead H G and McEuen P L 2010 *Nano Lett.* **10** 4869
[29] Wilson C M, Duty T, Sandberg M, Persson F, Shumeiko V and Delsing P 2010 *Phys. Rev. Lett.* **105** 233907
[30] Lin Z R, Inomata K, Koshino K, Oliver W D, Nakamura Y, Tsai J S and Yamamoto T 2014 *Nat. Commun.* **5** 4480
[31] Mahboob I, Flurin E, Nishiguchi K, Fujiwara A and Yamaguchi H 2011 *Nat. Commun.* **2** 198
[32] Dykman M I, Maloney C M, Smelyanskiy V N and Silverstein M 1998 *Phys. Rev. E* **57** 5202
[33] Eichler A, Heugel T L, Leuch A, Degen C L, Chitra R and Zilberberg O 2018 *Appl. Phys. Lett.* **112** 233105
[34] Hauer B D, Doolin C, Beach K S and Davis J P 2013 *Annals of Physics* **339** 181
[35] Moser J, Zhang C, Zhang Y B, Yang C, Lu H, Chen F N and Yan Y 2024 *Research Square*
[36] Castellanos-Gomez A, van Leeuwen R, Buscema M, van der Zant H S, Steele G A and Venstra W J 2013 *Adv. Mater.* **25** 6719
[37] Van Leeuwen R, Castellanos-Gomez A, Steele G A, Van Der Zant H S and Venstra W J 2014 *Appl. Phys. Lett.* **105** 041911

[38] Bunch J S, Van Der Zande A M, Verbridge S S, Frank I W, Tanenbaum D M, Parpia J M, Craighead H G and McEuen P L 2007 *Science* **315** 490

[39] Barton R A, Storch I R, Adiga V P, Sakakibara R, Cipriany B R, Ilic B, Wang S P, Ong P, McEuen P L, Parpia J M and Craighead H G 2012 *Nano Lett.* **12** 4681

[40] Morell N, Reserbat-Plantey A, Tsioutsios I, Schadler K G, Dubin F, Koppens F H and Bachtold A 2016 *Nano Lett.* **16** 5102

[41] Wang Z and Feng P X 2016 *Sci. Rep.* **6** 28923

[42] Blake P, Hill E W, Castro Neto A H, Novoselov K S, Jiang D, Yang R, Booth T J and Geim A K 2007 *Appl. Phys. Lett.* **91** 063124

[43] Roddaro S, Pingue P, Piazza V, Pellegrini V and Beltram F 2007 *Nano Lett.* **7** 2707

[44] Karabacak D, Kouh T and Ekinci K L 2005 *J. Appl. Phys.* **98** 124309

[45] Davidovikj D, Slim J J, Cartamil-Bueno S J, Van Der Zant H S, Steeneken P G and Venstra W J 2016 *Nano Lett.* **16** 2768

[46] Lu H, Yang C, Tian Y, Lu J, Xu F, Zhang C, Chen F, Ying Y, Schadler K G, Wang C, Koppens F H, Antoine R P and Moser J 2021 *Precision Engineering* **72** 769

[47] Han C, Wang M, Zhang B, Dykman M I and Chan H B 2024 *Phys. Rev. Research* **6** 023162

[48] Lapidus L J, Enzer D and Gabrielse G 1999 *Phys. Rev. Lett.* **83** 899

[49] Marthaler M and Dykman M I 2006 *Phys. Rev. A* **73** 042108

[50] Kim K, Heo M S, Lee K H, Jang K, Noh H R, Kim F D and Jhe W 2006 *Phys. Rev. Lett.* **96** 150601

[51] Chan H B and Stambaugh C 2007 *Phys. Rev. Lett.* **99** 060601

[52] Okamoto H, Gourgout A, Chang C Y, Onomitsu K, Mahboob I, Chang E Y and Yamaguchi H 2013 *Nat. Phys.* **9** 480

[53] Faust T, Rieger J, Seitner M J, Kotthaus J P and Weig E M 2013 *Nat. Phys.* **9** 485

[54] Zhang Z Z, Song X X, Luo G, Su Z J, Wang K L, Cao G, Li H O, Xiao M, Guo G C, Tian L, Deng G W and Guo G P 2020 *Proc. Natl. Acad. Sci. USA* **117** 5583

[55] Wang Y B, Zhang Z Z, Wu C X, Zhang Y S, Lei G S, Song X X and Guo G P 2025 *Chin. Phys. Lett.* **42** 070803

[56] Roychowdhury J 2015 *Proc. IEEE* **103** 1958

[57] Lee J, Wang Z, He K, Shan J and Feng P X L 2013 *ACS Nano* **7** 6086

[58] Jiang J W, Park H S and Rabczuk T 2014 *Nanoscale* **6** 3618

[59] Chen C, Rosenblatt S, Bolotin K I, Kalb W, Kim P, Kymissis I, Stormer H L, Heinz T F and Hone J 2009 *Nat. Nanotech.* **4** 861

[60] Zeng Q Y, Su G X, Song A S, Mei X Y, Xu Z Y, Ying Y, Zhang Z Z, Song X X, Deng G W, Moser J, Ma T B, Tan P H and Zhang X 2025 *Nat. Commun.* **16** 3793